Study of an oil sloshing problem: experiments and adaptive fixed-mesh ALE analyses

Ernesto Castillo[a], Marcela Cruchaga[a], Joan Baiges[b,c] and José Flores[a]
[a]Universidad de Santiago de Chile, Av Libertador Bernardo O'Higgins 3363, Santiago, Chile
[b]Universitat Politècnica de Catalunya, Jordi Girona 1-3, Edifici C1, 08034, Barcelona, Spain
[c]CIMNE – Centre Internacional de Metodes Numerics en Enginyeria, Gran Capità S/N 08034 Barcelona, Spain
ernesto.castillode@usach.cl (E. Castillo), marcela.cruchaga@usach.cl (M. Cruchaga), joan.baiges@upc.edu (J. Baiges) and jose.floresa@usach.cl (J. Flores)

Abstract

This work reports an experimental and numerical analysis of the sloshing of a squared tank partially filled with a domestic vegetable oil. The tank is subjected to controlled motions with a shake table. The free-surface evolution is captured using two experimental techniques: ultrasonic sensors and an image capturing method. The data obtained using these two techniques are compared between them and used to confirm the measurements. Only confirmed data within the error range are reported. Filling depth, imposed amplitude and frequency effects on the sloshing wave pattern are specifically evaluated. The experiments also reveal the nonlinear wave behavior. The material properties of the oil are also determined. The numerical model is based on a stabilized finite element method of the Variational Multi-Scale (VMS) type. The free-surface is captured using a level set technique particularly developed to be used with adaptive meshes in Arbitrary Eulerian Lagrangian reference frameworks. The experimental and numerical results are compared for different sloshing conditions near the first sloshing mode. The simulations satisfactorily match the experiments, providing a reliable tool for the analysis of this kind of problems.

Keywords: Sloshing, Experimental Validation, Arbitrary Lagrangian-Eulerian (ALE), Stabilized finite element methods, Adaptive Mesh

Contents

1. Introduction

Due to the importance of free-surface and two-fluid problems in many physical situations and engineering applications, such as, ship hydrodynamics, dam break, sloshing in tanks, shallow water, mold filling, or ink-jet analyses [1, 2, 3, 4], among others, the development of efficient and accurate numerical schemes capable of representing these types of phenomena is of major importance.

Interface problems, either, free-surface [5, 6], a thermally coupled analysis considering phase-change [7, 8], or even, solid mechanics problems with stresses location, damage or plasticity [9, 10, 11], are promising cases where the use of adaptivity is relevant because thin layers of the full domain contains the most important information of the global behavior of the problem. In this work an adaptive fixed-mesh ALE method is used to numerically approximate the sloshing of a rectangular tank partially filled with a domestic oil subjected to a controlled movement generated by a shake table. Numerical results are compared with experimental data obtained via image processing and the use of ultrasonic sensors.

Several approaches to study moving interfaces have been proposed over the years, and therefore, devising a single classifications that covers all of them is not an easy task. However, one of the most general classifications depends on the nature of the mesh used, which can be fixed or moving. A complete review of numerical methods used to solve free surface flow problems including experimental validation can be found in [4] and references therein.

In the computational fluid dynamics framework, the classical ALE approach has been proposed as a method where the computational mesh that covers the solved domain is deformed following the flow [12, 13]. In any moving discretization method, the accuracy of the method depends on the mesh distortion, which can be large in the type of sloshing problems dealt with in this paper, particularly when the excitation frequency is close to the natural frequency. Several methods have been devised to address this situation. The most common approach when an excessively distorted mesh is reached consists in computing a new mesh that ensures good quality form, and later, project the results from the deformed mesh to the new mesh [14, 15].

In [16], a fixed-mesh ALE approach for the numerical approximation of flows in moving domains was proposed. The key idea of this method consists in projecting the results of the ALE deformed mesh onto a fixed background mesh at each time step, prior to solving the flow equations. This procedure is known as a fixed mesh-ALE method, and in fact the ALE deformed mesh does not need to be explicitly solved. This fixed-mesh ALE approach was used satisfactorily both in free surface problems [17] as in the numerical simulation of floating solids [18], appearing as a powerful tool for the numerical approximation of moving domains. In [5], the fixed-mesh ALE method was coupled with an adaptive mesh algorithm giving place to a highly efficient and robust method. In that work, several numerical aspects were discussed in detail, such as, the global stabilization method used to ensure bounded pressure and to solve convective dominated flows

for equal interpolation spaces between velocity and pressure, and additionally, the stability terms designed to stabilize the ill-conditioning introduced by the cuts on the background finite element mesh.

Currently, big efforts are devoted to experimentally validate numerical models. To this end, controlled experiments are proposed to provide valuable data to be used for comparison with numerical results. In the present work, a novel sloshing experiment is reported and its numerical analysis is performed. The experiment consists of a square tank filled with a commercial vegetable oil and subjected to controlled imposed motion via a shake table. Sloshing experiments performed in water and their simulations were reported in [19, 20] using a similar layout. Those papers report experiments in rectangular tanks for a water filling depth of 100mm and the numerical modelling performed with fixed-mesh stabalised finite element formulations using free surface tracking and capturing techniques. In the present work, oil is used and different filling depths are investigated. The aim of this study is to measure wave height evolution during sloshing of square-section tank and evaluate its dependence on the filling depth. The measurements are made using two techniques to confirm and verify the experimental data. The modelling is performed with a VMS finite element adaptive level set formulation.

This work encompasses experimental and numerical analysis of an oil sloshing problem and its main contributions are:

- new experimental data are reported.
- a novel VMS finite element numerical model is presented and verified.
- comprehensive analysis of an oil sloshing problem is made.

The remainder of this work is organized as follows. Section 2 presents the governing equations and some general aspects of the numerical strategies used. In Section 3, the specific aspects of the stabilized finite element method used to solve free-surface problems using the level set method and the adaptive mesh approach are presented. The experimental study of an oil sloshing problem in square tanks is reported in Section 4, where the material properties are also determined. The modeling of the problem is presented in Section 5, comparison with experimental data validates the numerical model. Finally, conclusions are drawn in Section 6.

2. Problem statement and Galerkin finite element discretization

2.1. Boundary value problem

The conservation equations for momentum and mass in differential form for incompressible Newtonian fluids may be expressed for a fixed domain as:

$$\rho\frac{\partial \boldsymbol{u}}{\partial t} + \rho\boldsymbol{u}\cdot\nabla\boldsymbol{u} - \nabla\cdot(2\mu\nabla^s\boldsymbol{u}) + \nabla p = \boldsymbol{f}, \qquad \text{in } \Omega, t \in]0, t_f[\,, \tag{1}$$

$$\nabla\cdot\boldsymbol{u} = 0, \qquad \text{in } \Omega, t \in]0, t_f[\,, \tag{2}$$

where Ω is the computational domain of $\mathbb{R}^d$ occupied by the fluid, $d = 2$ or 3 are the space dimensions, $]0, t_f[$ is the time interval in which the problem is solved, ρ and μ denote the density and kinematic viscosity of the fluid, $p :]0, t_f[\to \mathbb{R}$ is the pressure field, $\boldsymbol{u} :]0, t_f[\to \mathbb{R}^d$ is the vector of velocity components, and $\boldsymbol{f} = \rho\boldsymbol{g}$ is

the gravity force vector, $\boldsymbol{g}$ is the gravity acceleration. As notation, $\nabla^s \boldsymbol{u}$ represents the symmetrical gradient of the velocity $\left(\nabla^s \boldsymbol{u} = \frac{1}{2}\left(\nabla \boldsymbol{u} + (\nabla \boldsymbol{u})^T\right)\right)$.

The above equations need to be solved together with initial and appropriate boundary conditions. We define the fluid stresses as

$$\boldsymbol{\sigma} = 2\mu \nabla^s \boldsymbol{u} - p\boldsymbol{I},$$

where $\boldsymbol{I}$ is the identity tensor. Usually boundary conditions in free-surface problems can be subdivided into Neumann and Dirichlet boundary conditions:

$$\begin{aligned} \boldsymbol{u} &= \boldsymbol{u}_D \qquad \text{on}\, \Gamma_D, \\ \boldsymbol{\sigma} \cdot \boldsymbol{n} &= \boldsymbol{h} \qquad \text{on}\, \Gamma_N, \end{aligned}$$

where $\boldsymbol{n}$ represents the outward unit normal vector, Γ_D is the Dirichlet boundary, and Γ_N is the Neumann boundary. When considering free-surface flows, the effect of any fluid outside the free-surface interface is neglected. Another usual assumption consists in neglecting the surface tension effects, which is reasonable in most engineering application. Under this assumption, the boundary condition we enforce in the free-surface interface, referred as $\Gamma_{\text{free}}(t)$, is a traction-free condition:

$$\boldsymbol{\sigma} \cdot \boldsymbol{n} = \boldsymbol{0} \qquad \text{on}\, \Gamma_{\text{free}}(t).$$

2.2. Fixed-Mesh ALE formulation

In free surface problems, the full domain represented by Ω can be split in two parts, the part of the domain effectively occupied by the fluid $\Omega_1(t)$ and the remaining $\Omega \backslash \Omega_1(t)$. The moving boundary of $\Omega_1(t)$ is known as the free surface, and it will be represented by $\Gamma_{\text{free}}(t)$. Note that both $\Omega_1(t)$ and $\Gamma_{\text{free}}(t)$ are time-dependent and can change in time. This movement of the domain can be represented using an ALE domain velocity $\boldsymbol{u}_\Omega(\boldsymbol{x}, t) \in \mathbb{R}^d$, where $\boldsymbol{x} \in \Omega$ are the spacial coordinates. Formally speaking, we can define the bijective mapping $\boldsymbol{\lambda}$, so that, for every point $\boldsymbol{X} \in \Omega$ and time instant t returns a point $\boldsymbol{x} = \boldsymbol{\lambda}(\boldsymbol{X}, t)$. Under this definition, the domain velocity can be defined as

$$\boldsymbol{u}_\Omega(\boldsymbol{x}, t) = \frac{\partial \boldsymbol{\lambda}(\boldsymbol{X}, t)}{\partial t}. \tag{3}$$

For an ALE approach, the domain velocity does not coincide in general with the velocity of the fluid in $\Omega_1(t)$. The effective conditions between domain velocity and velocity are defined by

$$\boldsymbol{n} \cdot \boldsymbol{u}_\Omega = \boldsymbol{n} \cdot \boldsymbol{u} \quad \text{in}\, \Gamma_{\text{free}} \cup \partial\Omega,$$

where $\boldsymbol{n}$ represents the outward normal of the point. In the rest of the domain, a smooth velocity consistent with these boundary conditions is defined.Under these definitions, the incompressible Navier-Stokes problem in the ALE frame of reference can be written as

$$\rho \frac{\partial \boldsymbol{u}}{\partial t}\bigg|_{\boldsymbol{\lambda}} + \rho\left(\boldsymbol{u}-\boldsymbol{u}_{\Omega}\right)\cdot\nabla\boldsymbol{u} - \nabla\cdot\left(2\mu\nabla^{s}\boldsymbol{u}\right) + \nabla p = \boldsymbol{f}, \qquad \text{in } \Omega, t\in\,]0,t_f[\,, \tag{4}$$

$$\nabla\cdot\boldsymbol{u} = 0, \qquad \text{in } \Omega, t\in\,]0,t_f[\,. \tag{5}$$

More details of this approach can be found in [21, 12, 16], where different ALE methods have been proposed for moving domains. In this work a Fixed-Mesh ALE method is used. The particularity of this method is that, after each discrete time integration scheme, the results are projected from the deformed mesh to the initially undeformed mesh, from which the simulation is continued. Thus, the method falls in the fixed-mesh method family, but it allows to properly track the movement of the domain using an ALE approach.

2.3. Variational form

Let us now consider the finite element approximation of the problem defined by (1)-(2). We define $\boldsymbol{\mathcal{V}} = \left(H^1\left(\Omega\right)\right)^d$ and $\mathcal{Q} = L^2\left(\Omega\right)/\mathbb{R}$, the interpolation spaces of the velocity and the pressure, respectively, $H^1\left(\Omega\right)$ is the space of functions whose distributional derivatives of order equal to one belong to $L^2\left(\Omega\right)$ vanishing on $\partial\Omega$. If we denote $\boldsymbol{\mathcal{X}} := \boldsymbol{\mathcal{V}}\times\mathcal{Q}$, the weak form of the problem consists in finding $\boldsymbol{U} = [\boldsymbol{u}, p] :]0,t_f[\,\rightarrow\boldsymbol{\mathcal{X}}$ such that the initial conditions are satisfied and

$$\rho\left(\frac{\partial \boldsymbol{u}}{\partial t}\bigg|_{\boldsymbol{\lambda}}, \boldsymbol{v}\right) + \left\langle\rho\boldsymbol{a}\cdot\nabla\boldsymbol{u}, \boldsymbol{v}\right\rangle + 2\mu\left(\nabla^{s}\boldsymbol{u}, \nabla^{s}\boldsymbol{v}\right) - \left(p, \nabla\cdot\boldsymbol{v}\right) = \left\langle\boldsymbol{f}, \boldsymbol{v}\right\rangle, \tag{6}$$

$$\left(\nabla\cdot\boldsymbol{u}, q\right) = 0, \tag{7}$$

for all $\boldsymbol{V} = [\boldsymbol{v}, q]\in\boldsymbol{\mathcal{X}}$, where it is assumed that $\boldsymbol{f}$ is such that $\left\langle\boldsymbol{f}, \boldsymbol{v}\right\rangle$ is well defined and $\boldsymbol{a} = \boldsymbol{u} - \boldsymbol{u}_{\Omega}$ is the advective velocity. Here $\left(\cdot,\cdot\right)$ stands for the $L^2\left(\Omega\right)$ inner product and $\left\langle\cdot,\cdot\right\rangle$ for the integral of the product of two functions, not necessarily in $L^2\left(\Omega\right)$

In compact form, the problem (6)-(7) can be written as:

$$\rho\left(\frac{\partial \boldsymbol{u}}{\partial t}\bigg|_{\boldsymbol{\lambda}}, \boldsymbol{v}\right) + B\left(\boldsymbol{a}; \boldsymbol{U}, \boldsymbol{V}\right) = \left\langle\boldsymbol{f}, \boldsymbol{v}\right\rangle, \tag{8}$$

where

$$B\left(\boldsymbol{a}; \boldsymbol{U}, \boldsymbol{V}\right) = \left(2\mu\nabla^{s}\boldsymbol{u}, \nabla^{s}\boldsymbol{v}\right) + \left\langle\rho\boldsymbol{a}\cdot\nabla\boldsymbol{u}, \boldsymbol{v}\right\rangle - \left(p, \nabla\cdot\boldsymbol{v}\right) + \left(\nabla\cdot\boldsymbol{u}, q\right).$$

Equation (8) needs to be complemented with appropriate initial and boundary conditions.

2.4. Galerkin finite element discretization and time discretization

The standard Galerkin approximation for the variational problem can be performed by considering a finite element partition $\mathcal{T}_h$ of the domain Ω. The diameter of an element domain $K\in\mathcal{T}_h$ is denoted by h_K and the diameter of an element partition is defined by $h = \max\left\{h_K \mid K\in\mathcal{T}_h\right\}$. Under the above considerations, we can construct conforming finite element spaces, $\boldsymbol{\mathcal{V}}_h\subset\boldsymbol{\mathcal{V}}$ and $\mathcal{Q}_h\subset\mathcal{Q}$ in the usual manner. If $\boldsymbol{\mathcal{X}}_h := \boldsymbol{\mathcal{V}}_h\times\mathcal{Q}_h$, and $\boldsymbol{U}_h = [\boldsymbol{u}_h, p_h]$, the Galerkin finite element approximation consists in finding $\boldsymbol{U}_h :]0,t_f[\,\rightarrow\boldsymbol{\mathcal{X}}_h$ such that

$$\rho\left(\left.\frac{\partial \boldsymbol{u}_h}{\partial t}\right|_{\boldsymbol{\lambda}}, \boldsymbol{v}_h\right) + B\left(\boldsymbol{a}_h; \boldsymbol{U}_h, \boldsymbol{V}_h\right) = \langle \boldsymbol{f}, \boldsymbol{v}_h \rangle, \tag{9}$$

for all $\boldsymbol{V}_h \in \boldsymbol{\mathcal{X}}_h$, and satisfying the appropriate initial and boundary conditions.

To discretize in time we use the second order backward difference scheme, defined as

$$\frac{\partial \boldsymbol{u}_h^{j+1}}{\partial t} = \frac{3\boldsymbol{u}_h^{j+1} - 4\boldsymbol{u}_h^{j} + \boldsymbol{u}_h^{j-1}}{2\delta t} + \mathcal{O}\left(\delta t^2\right), \tag{10}$$

where δt corresponds to the size of a uniform partition of the time interval $[0, T]$, while $\mathcal{O}(\cdot)$ represents the approximation order of the scheme. The superscript indicates the time step where the variable is being approximated, so that $\boldsymbol{u}^j$ is an approximation to $\boldsymbol{u}$ at time $t^j = j\delta t$. Note that this time marching scheme is independent of the method for spatial discretization.

With respect to the spacial discretization, it is well known that the standard Galerkin method fails when the nonlinear convective term dominates the viscous term. Another drawback is related to the discrete compatibility or inf-sup condition that must be satisfied by the $\boldsymbol{\mathcal{V}}_h \times \mathcal{Q}_h$ pair in order to have a well-posed problem with bounded pressure. These difficulties are overcome by using a stabilized formulation, as shown below.

3. Stabilized finite element method and adaptive mesh refinement approach

In this section we summarize the key ingredients of the adaptive fixed-mesh ALE approach used to solve the free surface problem. A more detailed description of the method can be found in [5].

3.1. Stabilized formulation

An equal order approximation for velocity and pressure does not yield a stable scheme even in a single fluid problem with fixed domain. A possible remedy to this situation is to enrich the finite element spaces for the velocity in order to satisfy the compatibility condition that defines the Navier-Stokes or even the Stokes problem. Another possibility consists in using stabilized formulations permitting any interpolation of the unknowns, which is the approach used in this work to ensure global stability. In short, a stabilized formulation consists in replacing B in (9) by another bilinear form B_h possibly mesh dependent, with enhanced stability properties.

The stabilized method used in this work is based on the variational multi-scale (VMS) approach introduced in [22]. The basic idea is of this method is to approximate the effect of the components of the solution of the continuous problem that cannot be solved by the finite element mesh, called the sub-scale components. In the end, the problem can be written only in terms of the finite element component, maintaining the number of the unknowns of the Galerkin case with the possibility to solve convective dominant cases with equal order interpolation for velocity and pressure. A detailed derivation of the method can be found in [23] for the Navier-Stokes problem. Here we just state the method for the problem defined by (6)-(7). After some approximations, this method consists in finding $\boldsymbol{U}_h :]0, t_f[\to \boldsymbol{\mathcal{X}}_h$ such that

$$\rho\left(\frac{\partial \boldsymbol{u}_h}{\partial t}, \boldsymbol{v}_h\right) + B\left(\boldsymbol{a}_h; \boldsymbol{U}_h, \boldsymbol{V}_h\right) + S_1\left(\boldsymbol{a}_h; \boldsymbol{U}_h, \boldsymbol{V}_h\right) + S_2\left(\boldsymbol{U}_h, \boldsymbol{V}_h\right) = \langle \boldsymbol{f}, \boldsymbol{v}_h \rangle, \tag{11}$$

for all $\boldsymbol{V}_h \in \boldsymbol{\mathcal{X}}_h$, where

$$
\begin{aligned}
S_1\left(\boldsymbol{a}_h;\boldsymbol{U}_h,\boldsymbol{V}_h\right) =& \sum_K \alpha_1 \Big\langle \boldsymbol{f} - \rho\frac{\partial \boldsymbol{u}_h}{\partial t} - \rho\boldsymbol{a}_h\cdot\nabla u_h + \mu\triangle\boldsymbol{u}_h - \nabla p_h, \\
& -\rho\boldsymbol{a}_h\cdot\nabla\boldsymbol{v}_h - \mu\triangle\boldsymbol{v}_h - \nabla q_h\big\rangle_K\,, \\
S_2\left(\boldsymbol{U}_h,\boldsymbol{V}_h\right) =& \sum_K \alpha_2 \left\langle \nabla\cdot\boldsymbol{u}_h, \nabla\cdot\boldsymbol{v}_h\right\rangle_K,
\end{aligned}
$$

are the stabilization terms added to the Galerkin formulation and $\boldsymbol{\alpha}$ is a matrix computed within each element, called matrix of stabilization parameters, which among other things gives dimensional consistency to the added terms. Note that both terms are residual based; the first term depends on the residual of the momentum equation and the second one on the continuity equation, and therefore, the stabilized method is consistent by construction. Based on [24, 25], we define

$$
\boldsymbol{\alpha} = \operatorname{diag}\left(\alpha_1\boldsymbol{I}_d, \alpha_2\right), \tag{12}
$$

with $\boldsymbol{I}_d$ the identity on vectors of $\mathbb{R}^d$ and the parameters α_i, $i = 1, 2$, are computed as

$$
\alpha_1 = \left[c_1\frac{\mu}{h_1^2} + c_2\frac{\rho\left|\boldsymbol{a}_h\right|}{h_2}\right]^{-1}, \tag{13}
$$

$$
\alpha_2 = \frac{h_1^2}{c_3\alpha_1}, \tag{14}
$$

In these expressions, h_1 corresponds to a characteristic element length calculated as the square root of the element area in a two-dimensional case and the cubic root of the element volume in 3D, and h_2 corresponds to another characteristic length calculated as the element length in the streamline direction. The constants c_i, $i = 1, 2, 3$ are algorithmic parameters in the formulation. The values used in this work are $c_1 = 12$, $c_2 = 2$, and $c_3 = 4$, which can be derived from the numerical analysis of the one-dimensional convection-diffusion-reaction problem. These values have proven to be robust in different problems and for different applications.

The above stabilized formulation ensures global stability except for the ill-conditioning and unstable behavior caused by the sub-integration in the elements cut by the free surface. In order to overcome this local instability a method known as the ghost penalty stabilization is used. This method ensures the control of a given field in the cut elements without harming the convergence rate of the numerical formulation. See [26] and [27]where the method was first applied for fluid flow problems. It is important to note that the ghost penalty stabilization method affects only the part of the domain in the layers of elements cut by the free surface. In short, the terms added to 3.1 are

$$
\begin{aligned}
S_{ghost}\left(\boldsymbol{a}_h;\boldsymbol{U}_h,\boldsymbol{V}_h\right) =& \sum_K \left(c_4 h_1^2\alpha_1^{-1}\right)\left\langle\nabla\boldsymbol{v}_h, P_{\boldsymbol{u}}^{\perp}\left(\nabla\boldsymbol{u}_h\right)\right\rangle_{K(\Omega_{cut}(t))} \\
& + \sum_K \left(c_5\alpha_2\right)\left\langle\nabla q_h, P_p^{\perp}\left(\nabla p_h - \boldsymbol{f}\right)\right\rangle_{K(\Omega_{cut}(t))},
\end{aligned} \tag{15}
$$

where $\Omega_{cut}\left(t\right)$ represents the domain of the K element cut by the free surface $\Gamma_{\text{free}}\left(t\right)$, c_4 and c_5 are algorithmic

constants, both taken as 0.1 in this work, and $P^{\perp}$ represents the orthogonal projections in the cut elements, that are defined as

$$\begin{aligned} P_{\boldsymbol{u}}^{\perp}\left(\nabla \boldsymbol{u}_h\right) =& \nabla \boldsymbol{u}_h - P_{\boldsymbol{u}}\left(\nabla \boldsymbol{u}_h\right), \\ P_p^{\perp}\left(\nabla p_h - \boldsymbol{f}\right) =& \left(\nabla p_h - \boldsymbol{f}\right) - P_p\left(\nabla p_h - \boldsymbol{f}\right), \end{aligned}$$

where $P_{\boldsymbol{u}}$ represents the $L^2(\Omega)$ projection onto $\boldsymbol{\mathcal{V}}_h$, and P_p the $L^2(\Omega)$ projection onto $\mathcal{Q}_h$. Note that the $L^2(\Omega)$ projection is not the only possibility (see [28] for other options of interpolators used in the ghost penalty method). A more detailed description of this stabilization technique can be found in [5]

3.2. Tracking of the interface

The common option to solve free surface problems using fixed mesh approaches is to solve a two-fluid flow problem. However, in a water-air (or oil-air) interaction problem, the effect of air on water can be neglected, and thus air does not need to be modelled. This allows one to solve a single fluid flow problem. The key point to do this is to disconnect both domains, which is achieved by imposing a traction-free condition over the interface. Using this approach, the Navier-Stokes problem is solved only for the water or oil domain. In the air domain, any smooth extrapolation function can be used for the velocity and pressure fields. In this work, a Stokes problem is used in the air domain.

For the tracking of the two fluids interface, the level set method is used. It is based on the pure advection of a smooth function, commonly defined as $\phi(\boldsymbol{x}, t)$, over the whole domain Ω. This function allows one to define the position of the front of the interface, by the isovalue $\phi(\boldsymbol{x}, t) = \phi_c$, usually taken as $\phi_c = 0$.

The conservation of ϕ in any control volume $V_t \subset \Omega$ which is moving with a divergence free velocity field $\boldsymbol{u}$, can be defined in an Arbitrary-Lagrangian-Eulerian (ALE) frame by the following equation

$$\frac{\partial \phi}{\partial t} + \boldsymbol{a} \cdot \nabla \phi = 0, \qquad \text{in } \Omega, t \in]0, t_f[, \tag{16}$$

with the corresponding initial and boundary conditions, and the advection velocity defined as $\boldsymbol{a} = \boldsymbol{u} - \boldsymbol{u}_{\Omega}$.

For the numerical solution of the level set equation, standard numerical techniques are used. In this work, the level set equation (16) is solved by using the classical SUPG method [29] to stabilize the convective nature of the equation. The time derivative is discretized in the same way as in the momentum equation described in subsection 2.4.

As the level set interface evolves in time, it will intersect the elements of the finite element mesh in an arbitrary manner. To properly integrate the physical properties in the computational domain, a modified integration rule is used in the elements cut by the interface [6, 5]. The use of the enhanced integration allows to impose the zero traction boundary condition correctly at the exact position of the interface.

The advection of the level set function does not guarantee global mass conservation. Depending on the space-time discretization employed, the amount of volume loss of the solved fluid can be important. In a sloshing problem thousands of time steps needs to be solved, and therefore, the use of a mass conservation scheme is convenient. In the present work, we use a very simple method to ensure the global mass conservation,which consists in measuring the total mass at the end of each time step and compute the amount of mass lost, and then accordingly displace the level set function in a uniform, global manner in the direction orthogonal to the free-surface in order to recover the lost mass (see [5] for more details)

3.3. Adaptive approach

A key ingredient in the numerical simulations presented in this work is an adaptive mesh refinement strategy that tracks the position of the free surface, and allows one to achieve accurate solutions by using reasonably small number of elements. For this, the Fixed-Mesh ALE method is coupled with the parallel adaptive mesh refinement library `RefficientLib` [30]. The particularity of applying adaptive refinement approaches to free surface problems is that in many cases, the precision of the numerical simulation depends mostly on the accuracy with which the interface between the two materials is tracked [5]. Thus, an adaptive mesh refinement criterion based on layers of elements around the fluids interface is used in this work.

In the present work, the mesh refinement algorithm proposed in [30, 5] is used to validate the numerical results with the experimental data also proposed in this work. The adaptive mesh refinement algorithm used in the work is based on layers of elements of different size. In general, a free surface problem could be divided into four zones: the most important one is the region (a layer) close to the free surface that contains elements occupied by the fluid as well as elements outside of the fluid. A second layer could be a region located neither so far nor so close to the free surface and adjacent to the first layer. A third zone is represented by the region far away from the free surface, but inside of the fluid, and finally, a fourth zone is represented by the region far away from the free surface but outside the fluid.

The adaptive mesh refinement algorithm for free surface problems proposed in this work is based on three positive integers parameters that refer to the level of refinement in each of these layers. Calling the parameters as a, b and c, we show as the algorithm work for a sloshing case. Figure 1 shows the first eight time steps of a sloshing case, starting from an extremely coarse mesh (left top) called M_0 composed of elements of size h_0.

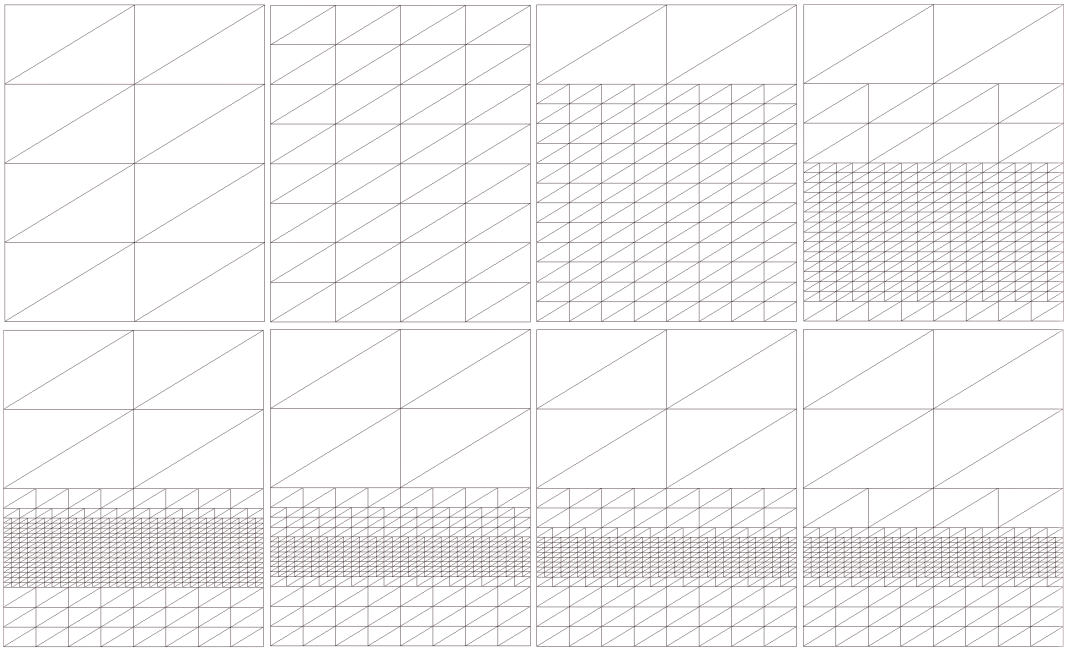

Figure 1: Adaptive mesh refinement initialization for a free surface problem.

For the case shown in Fig. 1, the integer parameters were set as $a = 2$, $b = 2$ and $c = 8$. The first value refers to the level of refinement taking as reference the original mesh M_0. The value $a = 2$ means that the

elements far away from the free surface, but inside of the region occupied by the fluid have two levels of refinement, and therefore, the element size is a quart of the originals ($h_e = \frac{1}{4}h_0$). The value $b = 2$ refers to the level of refinement of the elements cut by the fluid interface and very close to the free-surface both out as in of the fluid, giving place to elements of size equal to 1/16 of the originals. The c parameter allows us to define the number of element layers that conform the zone where the finest mesh is used ($h_e = 1/16$). For $c = 8$ layers of, we have 8 elements of size $h_e = \frac{1}{16}h_0$ of the original one associated to M_0.

In Fig. 2, an example of the adaptive mesh refinement algorithm is presented for a sloshing case. In this figure the capability of the algorithm for refining and coarsening the mesh in a time dependent problem is shown.

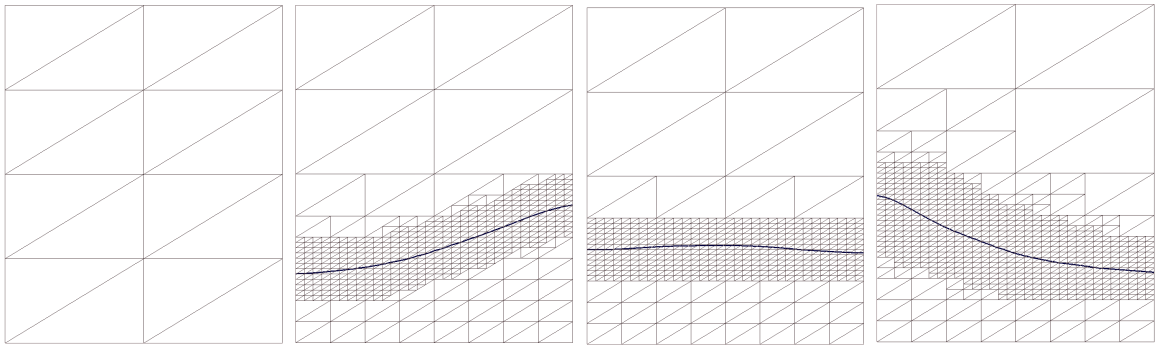

Figure 2: Free surface evolution using the adaptive mesh approach for a case near to the first mode.

In this work, we make a mesh convergence study using a fixed mesh size, but changing the thickness of the region of smallest elements. In other words, we leave the values of a and b fixed, and change the value of the parameter c, as will be described in Section 5.

4. Experimental work

An acrylic tank filled with commercial vegetable oil is mounted on a shake table to be subjected to controlled vibrations. The experimental setup is shown in Figure 4. The dimensions of the square section tank are shown in Figure 3, where H is the oil depth. The shake table is actuated by a motor that makes a screw rotate, producing a one-dimension time-varying motion. The amplitude and frequency of the imposed motion can be set by a user interface tool (see Quanser User Manual [31] for further details). An experimental study of water sloshing in a rectangular tank has been also presented in [19]. In such a work, experiments using only one water depth were reported, using a unique procedure to measure wave heights. The present work studies the effect of the filling depth on the wave heights for the sloshing of oil in square tanks. Moreover, two different techniques for measuring wave heights are used with the aim to confirm and to complete the experimental data.

The wave height is measured at four control points (CP in Figure 3) using ultrasonic sensors. According to the output configuration used, this instrument has a resolution of 1mm for the adopted output response time of 2.5ms [32]. The readings made by the ultrasonic sensors, based on the wave-beam's transit time, can be distorted due to the shape of the free surface, e.g., a surface with high slope can not be correctly recognized. Other facts also affects the interface detection. The ultrasonic beam can not be interfered by the walls of the

container. In addition, the sensors have a distance range from the emitting point and the surface where the surface can be detected. These facts are taken into account to define the sensors' location in the experiment. Because of these aspects, under certain experimental conditions, the water level can not be measured using the ultrasonic sensors, or the quality of the obtained data can not be assured. It could typically happen when sharp waves or strong $3D$ effects evolves and the free surface is highly distorted (even when not separation is obtained). However, the ultrasonic sensors provides information for long terms analyses. The experiments are also recorded using a high speed camera (AOS [33]). This procedure is limited to the total time that can be registered. In the present study 10s during the steady state time-periodic regime were recorded with a resolution of 800×800 pixels at 120 frames per second. To process the videos a Python home-made code has been developed using the OpenCV library [34]. This code handles a video file and treats it frame-by-frame, taking two regions of interest (ROI) coherent with the ultrasonic sensors positions. The horizontal center of these ROIs is the control line (CL) where the wave height is measured, and its position changes restricted to the tank's marker. Then, a color mask is applied to distinguish the fluid from the background and so find the pixel correspondence with the free surface. A scheme of the procedure is shown in the Figure 5. The error bound in the measurements is 1.1mm. The measurements obtained using this procedure help to verify and to complete the experimental data.

The experimental work is focused on the wave height evolution for different oil filling depths, and encompass experimental sweep analyses. In particular, four oil depths H have been used: 100mm, 150mm, 200mm and 250mm. The imposed motions have amplitudes A of 5mm, 7.5mm and 10mm, while the imposed frequency f has been defined in terms of the analytic first natural frequency for non-viscous fluids [35], the geometry of the tank. and the liquid's depth (see Table 1). In this work, the values of the imposed frequency goes from $0.55 \times fn$, up to $1.45 \times fn$. The first natural frequency of the oil sloshing has also been determined experimentally by examination of the damped decaying regime via a Fast Fourier Transform. From these analyses, the natural frequencies coincide with the analytic expression, showing its independence from the fluid's viscosity for the studied cases, see Figure 6.

H[mm]	100	150	200	250
$f_{n,a}$[Hz]	1.46998	1.58511	1.62962	1.62962
where $f_{n,a} = (g/(4\pi l)\tanh(\pi H/l))^{1/2}$ with $l = 288$mm				

Table 1: Analytic first natural frequencies.

To illustrate the typical free surface responses, the wave height evolution at CP1 for the entire analysis using $H = 100$mm, $A = 7.5$mm and $f = 1.69$Hz ($1.15 \times fn$, $fn = 1.469$Hz) is presented in Figure 7. The initial transient, time-periodic and damped decaying regimes can be clearly seen. It should be noted that the steady state time-periodic regime is reached 20s after starting the motion. Figure 8 reports the wave evolution during the time-periodic regime for the same case. The ultrasonic sensors and image capturing measurements practically coincide.

As already mentioned, in some cases there are difficulties to capture the free surface evolution using sensors. The wave evolution during the time-periodic regime for $H = 100$mm, $A = 7.5$mm and $f = 1.25$Hz ($0.85 \times fn$, $fn = 1.469$Hz) is plotted in Figure 9. The signals of the sensor are discontinuous in time. These signals can be confirmed only by parts using the motion capturing measurements. In this case, only signals obtained from images will be used to evaluate maximum and minimum wave amplitudes during the

time-periodic regime.

Moreover, sensors located at CP3 and CP4 helps to detect the evolution of 3D effects when signals at CP1 and CP3 (or CP2 and CP4) are different, while for 2D motions CP1 and CP3 (or CP2 and CP4) practically coincide.

Figure 10 presents the maximum and minimum wave amplitudes $\eta^{+/-}$ during the time-periodic regime for the studied cases. The amplitudes are presented organised by H. From these data different aspects can be observed. Maximum and minimum amplitudes of the waves are not symmetric, i.e., the absolute maximum is higher than the absolute minimum, denoting the nonlinear behaviour in the wave pattern. Smaller imposed amplitudes promote lower wave amplitudes. Although wave amplitudes can not be measured during first resonance, the effect that the first natural frequency increases with depth is apparent.

Figure 11 reproduces the same previously reported data, but organized by the imposed amplitude and referred to the relative imposed frequency $f_r = f/f_n$. This figure shows that the wave amplitudes tends to be similar when the liquid depth increases.

The ratio between maximum and minimum wave height is plotted in Figure 12. The error bars are also included, showing the influence of the low wave amplitudes measured with the declared error in the computation of the ratio. The nonlinear behaviour, represented by ratios not equal to one, is apparent in the figure. High nonlinearities are found near the first resonant frequency and at low filling depth. The ratios increase when the imposed amplitude increases. It can also be seen that near the resonant frequency the ratios remain practically constant. The ratios decrease when the filling depth increases, and they tend to be similar when the filling depth increases, denoting that the wave patter is practically invariant at large filling depths.

Numerical and experimental results are presented in Section 5 to validate the proposed methodology for analyzing free surface flow problems. On the contrary, numerical solutions confirm image measurements.

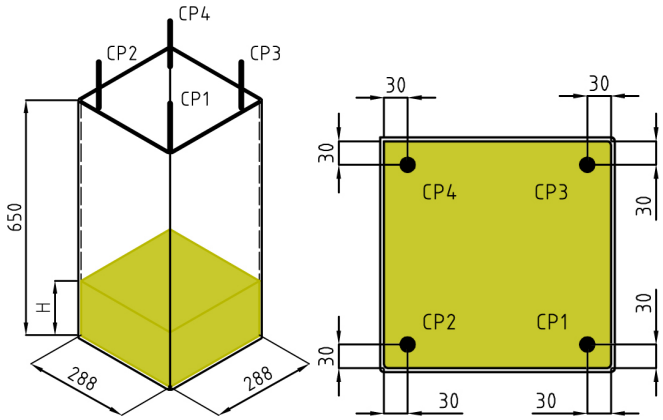

Figure 3: Isometric view of the tank used, with its internal dimensions and the four control points (left) and top view of the same tank, where the distances from the control points to the tank walls are shown (right). The dimensions are in mm.

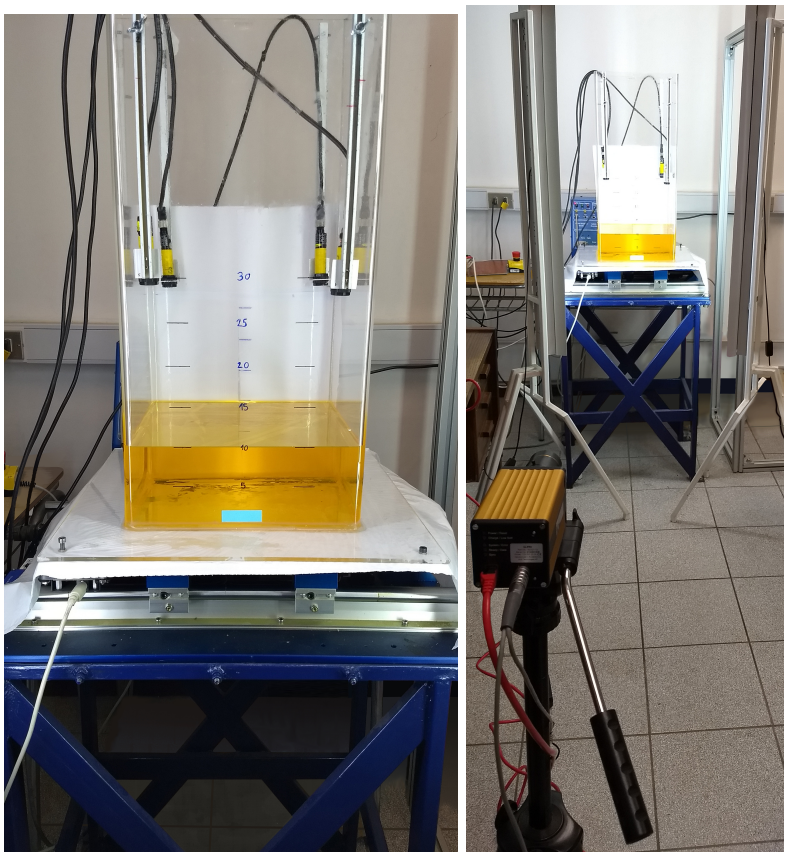

Figure 4: Experimental setup of the shake table loaded with the tank partially filled with vegetable oil, and the ultrasonic sensors installed at the specified control points (left) and overall view (right).

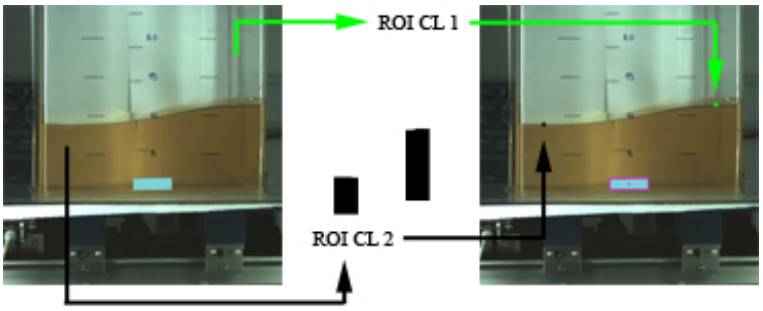

Figure 5: Scheme of the procedure of the developed code to process the high-FPS recorded videos. On the left side the input frame is shown, while on the right side shows the output frame with the wave height and tank markers.

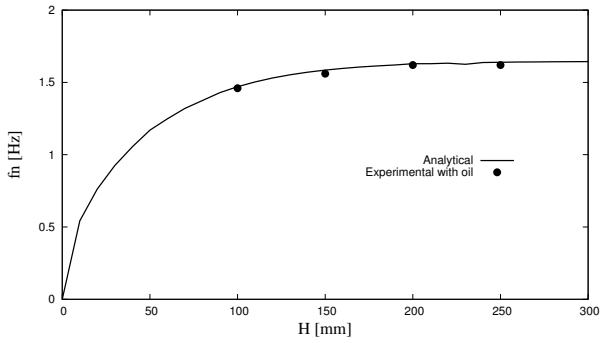

Figure 6: First natural frequency, dependence on liquid depth.

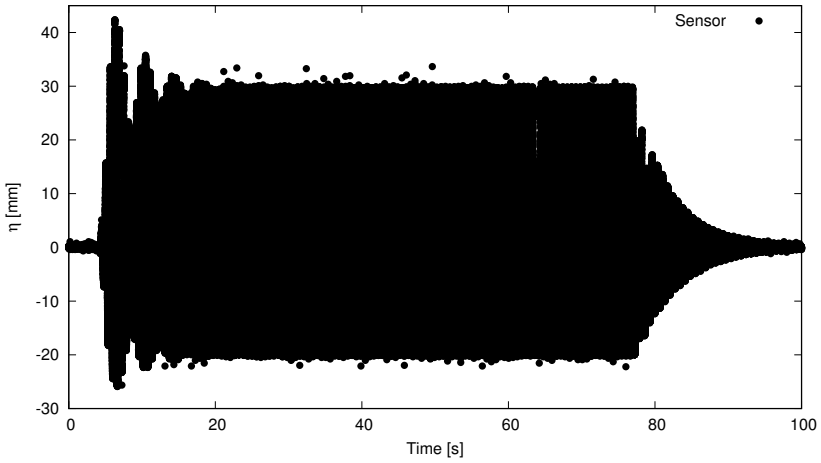

Figure 7: Wave evolution at CP1 obtained using ultrasonic sensors for H=100 mm, A= 7.5 mm and f=1.69 Hz.

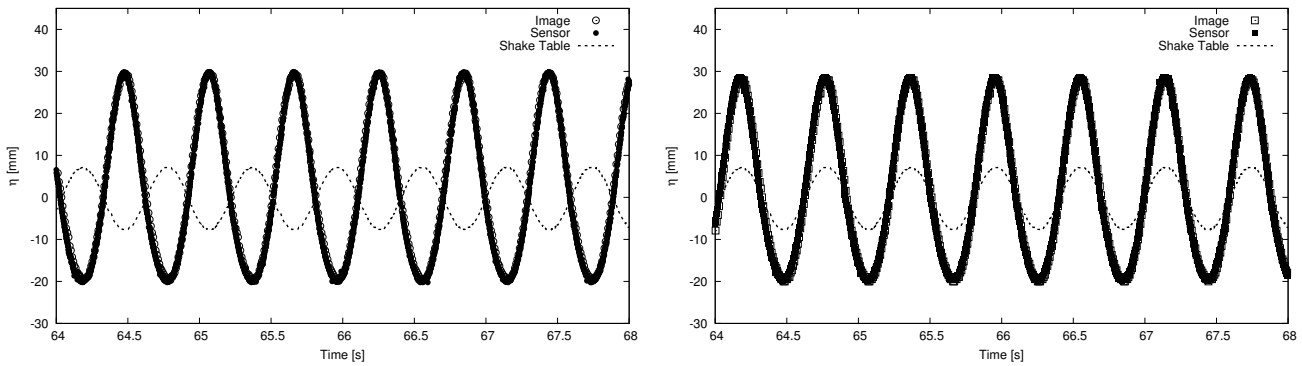

Figure 8: Experimental data, wave evolution during steady-state time-periodic regime at CP1 (left) and CP2 (right), comparison between sensors and image capturing measurements for H=100 mm, A= 7.5 mm and f=1.69 Hz.

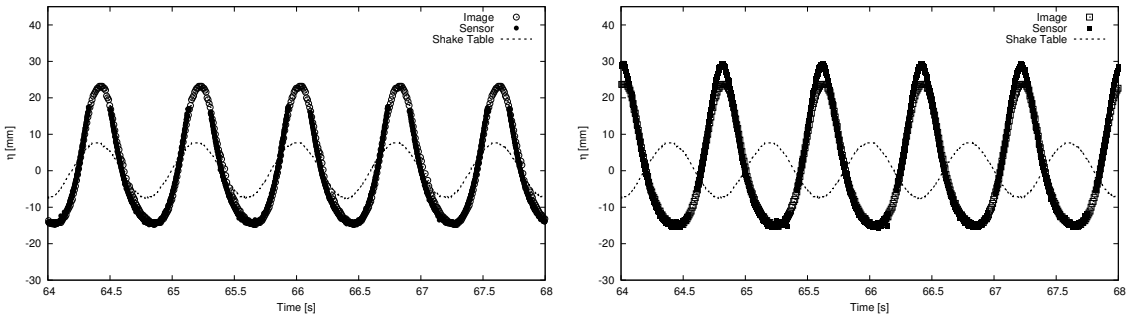

Figure 9: Experimental data, wave evolution during steady-state time-periodic regime at CP1 (left) and CP2 (right), comparison between sensors and image capturing measurements for H=100 mm, A= 7.5 mm and f=1.25 Hz.

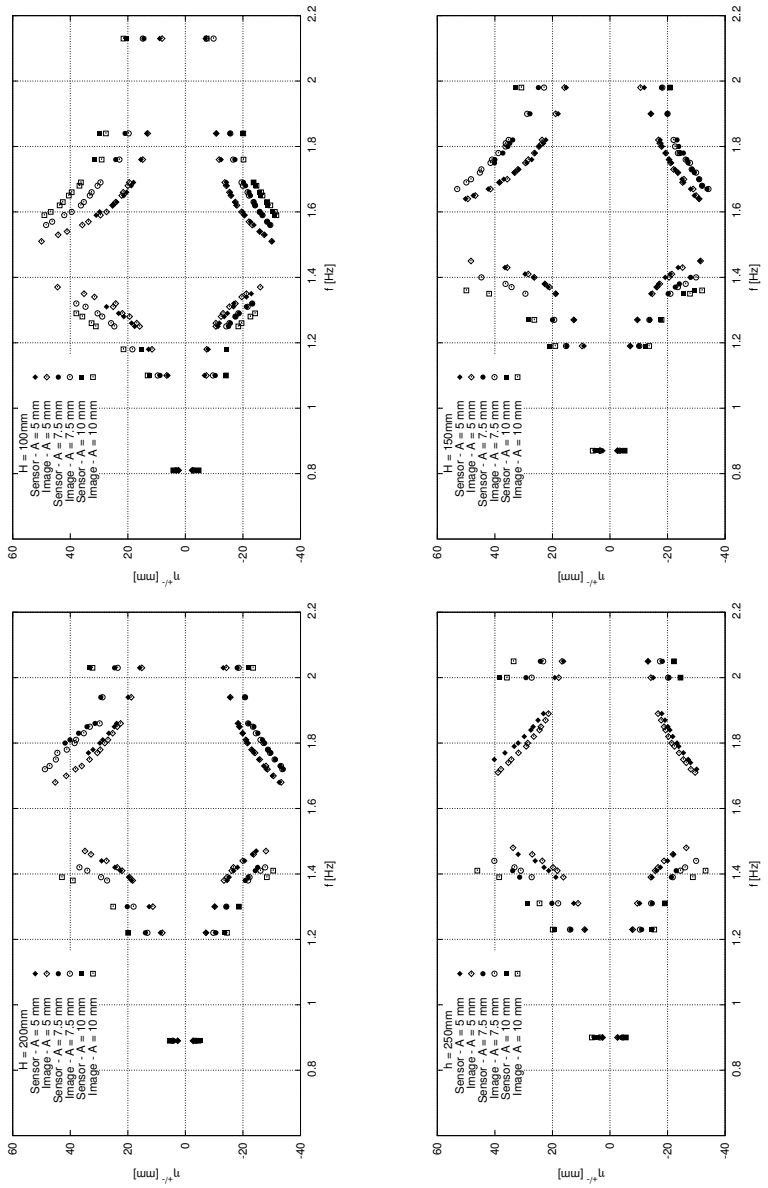

Figure 10: Experimental sweep analysis: maximum and minimum wave amplitudes at CP1 for each oil depth H, ultrasonic and image data.

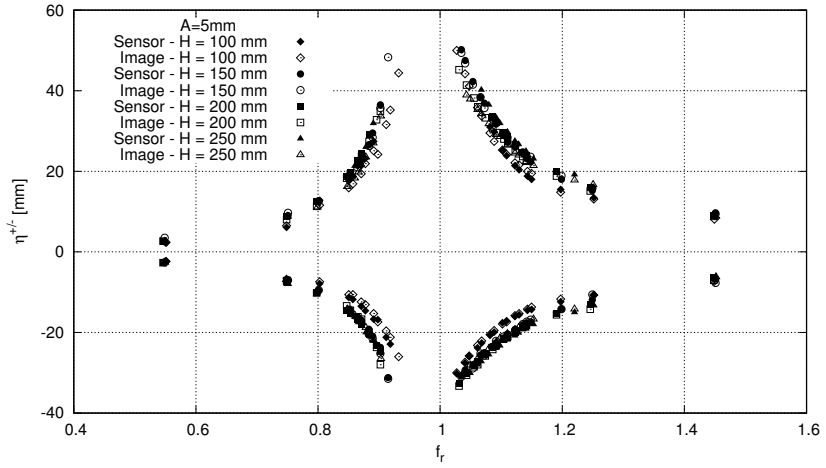

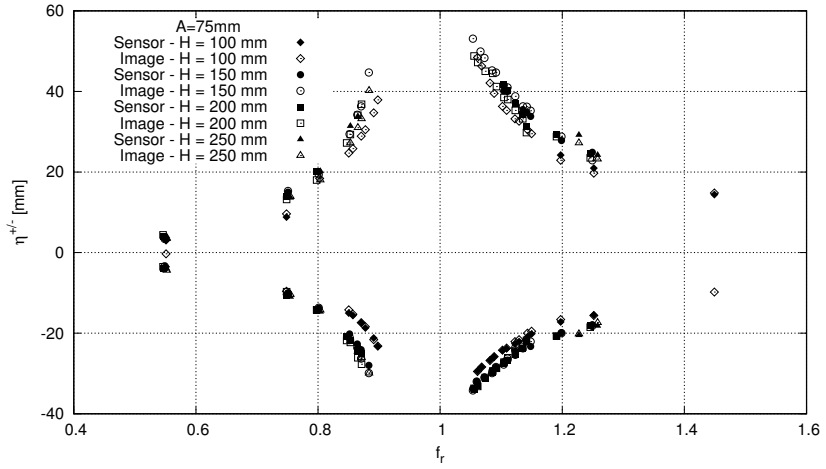

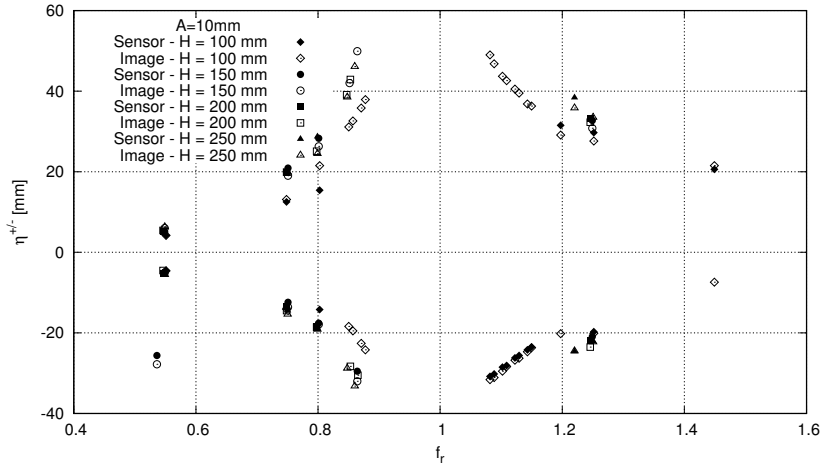

Figure 11: Experimental sweep analysis for each imposed motion amplitude: maximum and minimum wave amplitudes at CP1 vs. relative imposed frequencies, ultrasonic and image data.

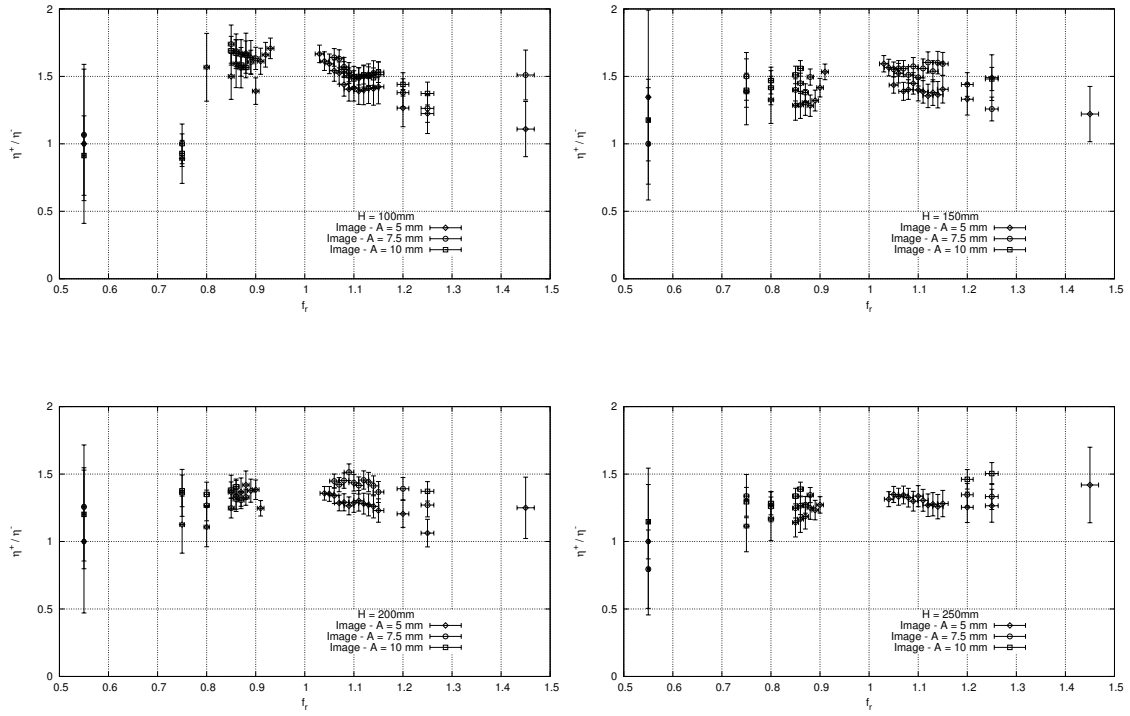

Figure 12: Experimental sweep analysis: ratio between maximum and minimum wave amplitudes at CP1 for each oil depth H, image data.

4.1. Material characterization

The properties of the vegetable oil used are determined experimentally. Figure 13 reports the density and the viscosity obtained. From the study reported in [36], the viscosity of vegetable oils depends on temperature according to the expression summarized in Table 2. The experimentally determined coefficients are reported in Table 2. The obtained viscosity behaviours are similar to those obtained for sunflower and corn oils in [36].

$\mu(T) = (a + bT)e^{c+d/T+e/T^2}$ mPas				
a	b	c	d	e
2.1665	$4.1832E-03$	6.3958	-6.0213×10^3	$1.4937E \times 10^6$

Table 2: Temperature-dependent viscosity.

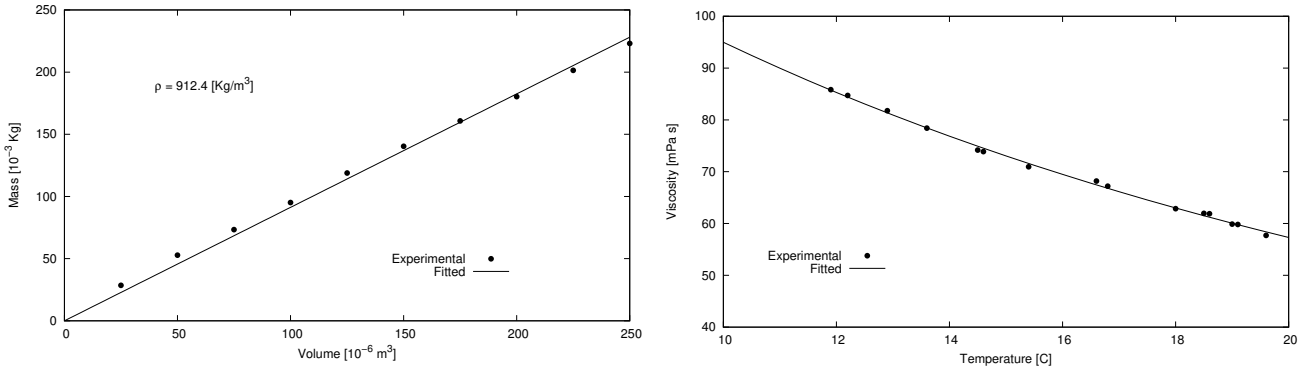

Figure 13: Material properties.

5. Modelling the experiments

The present Section reports the numerical analyses made using the proposed fully formulation described in Section 2. The numerically studied cases are those with $H = 100$mm and $A = 7.5$mm at different imposed frequencies. In all cases the properties of the fluid were set as $\rho = 912.4$kg/m^3 and $\mu = 71$mPas.

Figure 17 summarizes the numerical results computed using different meshes and time step sizes in comparison with experimental data. The three meshes used (named as $M1$, $M2$ and $M3$), are shown in Figure 14. Note that the element size is the same in all the meshes, but the number of elements in the layer of finest elements changes between them. In this work we study the effect of this parameter on the convergence of the results using the experimental data. In mesh $M1$ we set the c parameter described in sub-Section 3.3 as $c = 8$. For mesh $M2$ the value was set at $c = 10$ and for $M3$ $c = 12$.

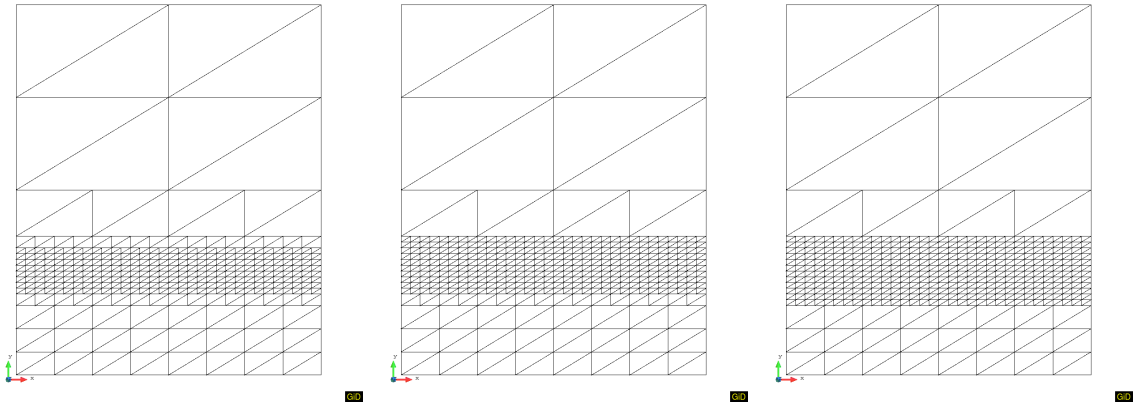

Figure 14: Meshes used for the sloshing problem: $M1$, $M2$ and $M3$ from left to right.

Simulations using $M1$ and time steps of 0.005s, 0.0025s and 0.00125s reveal practically independent time step size results (see Figure 17, right). The mesh convergence analysis, made using a time step of $0.00125s$, presents improved results when finer meshes are used (see Figure 17, left). Note that for $M3$ the numerical results fit well with the experimental data in the zone near the first mode. These results corroborate that

the most efficient way to solve a problem of free surface is with adaptability. Additionally, it is evident that the fixed mesh ALE approach is a robust method to solve cases even close to resonance.

Figures 15 and 16 report experimental data and numerical results during time-periodic and transient regimes respectively. Figure 15 illustrates that wave height evolution at CP1 is in phase with shake table motion for frequencies lower than the first natural frequency, while the phase is 2π at frequencies greater than the first frequency. Moreover, as expected, the wave height evolution at CP2 has a 2π phase with respect to wave height evolution at CP1.

Snapshots from the videos and simulations are also plotted in Figures 18 to 21 for imposed frequencies of 1.25 Hz, 1.32 Hz, 1.62 Hz, and 1.69 Hz.

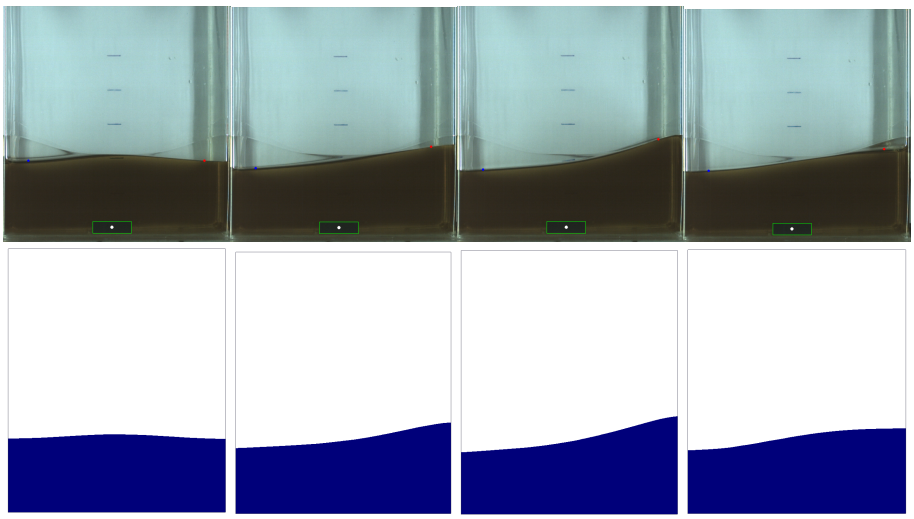

Figure 18: Free surface evolution in a period for $f = 1.25$ Hz ($f_r = 0.85$).

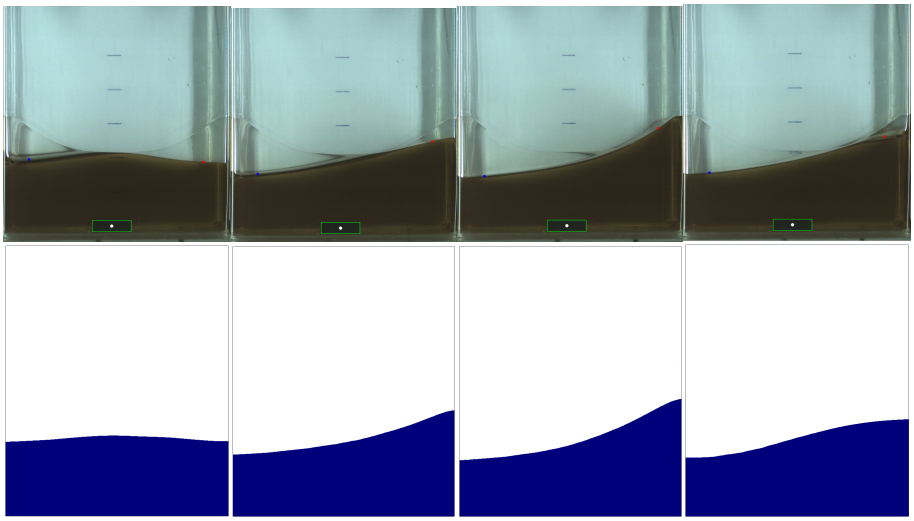

Figure 19: Free surface evolution in a period for $f = 1.32Hz$ ($f_r = 0.9$).

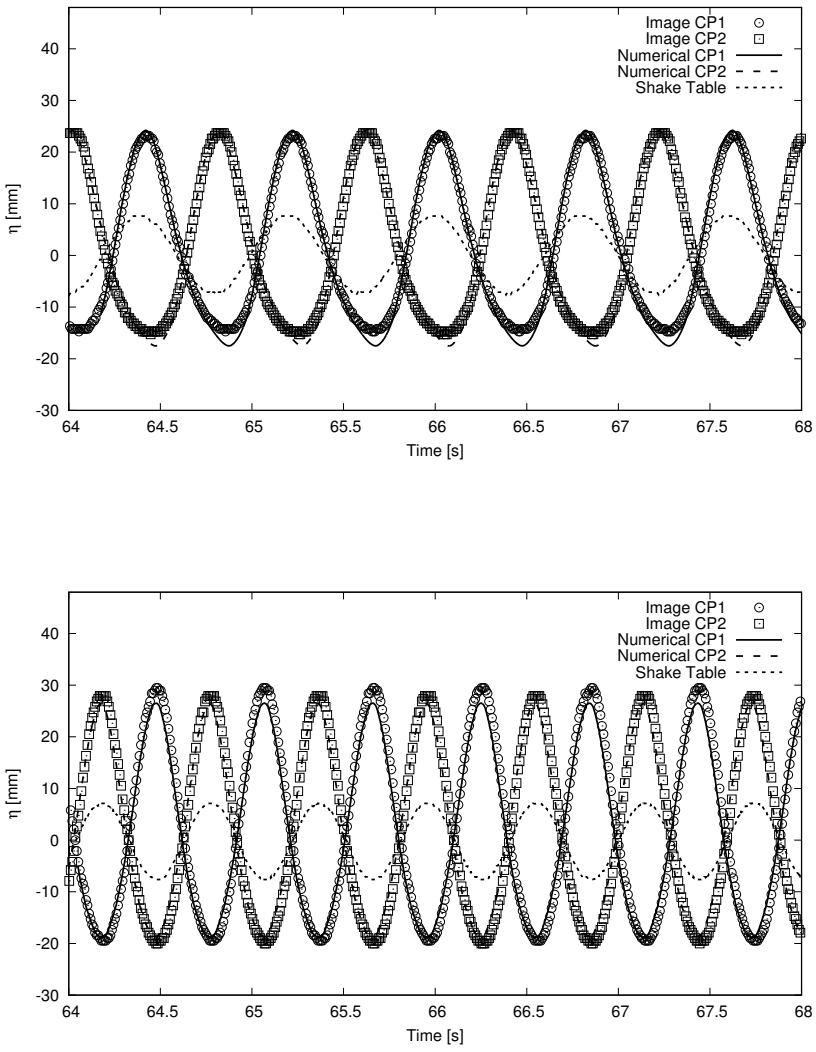

Figure 15: Experimental data vs. numerical results for H=100 mm, A= 7.5 mm, f=1.25 Hz (top) and f=1.69 Hz (bottom) during time-periodic regime.

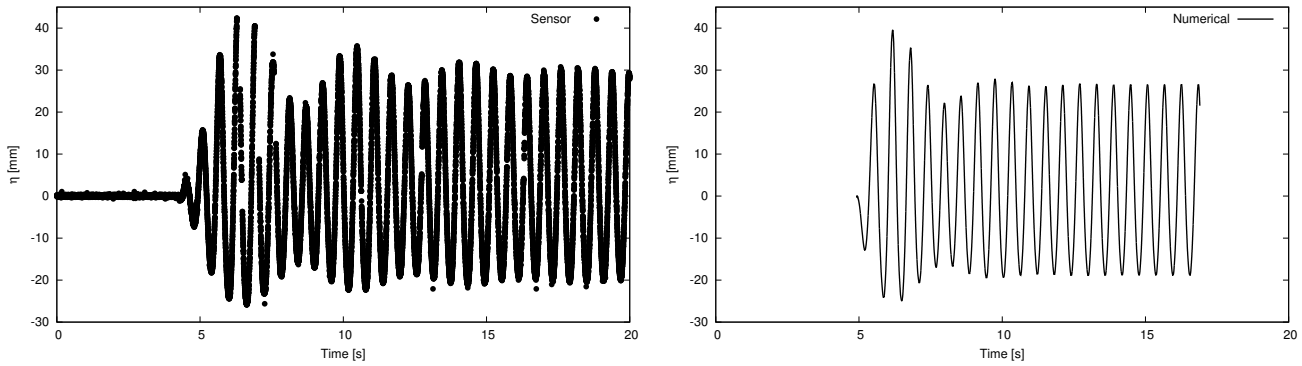

Figure 16: Experimental data (left) vs. numerical results (right) for H=100 mm, A= 7.5 mm and f=1.69 Hz during initial transient regime.

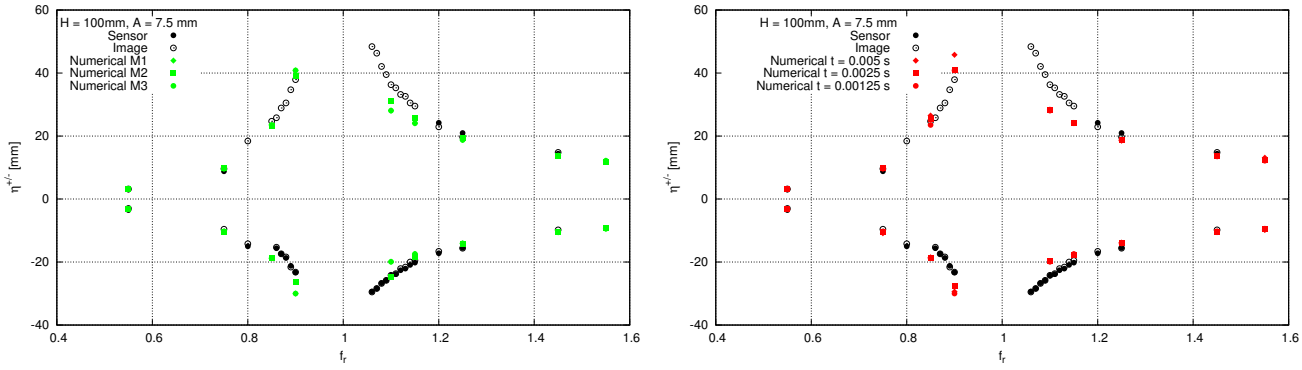

Figure 17: Frequency sweep analysis: experimental data vs. numerical results for H=100 mm and A= 7.5 mm. Maximum and minimum wave amplitudes at CP1. Mesh (left) and time step (right) convergence analyses.

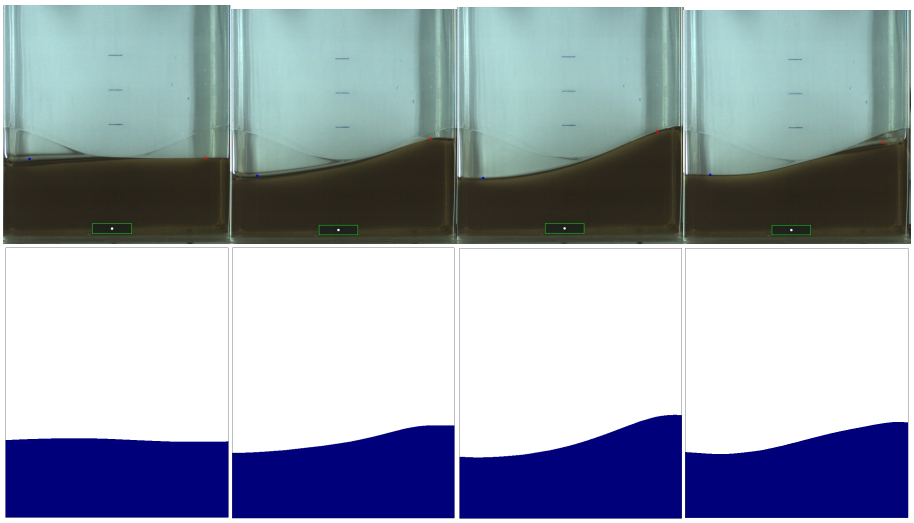

Figure 20: Free surface evolution in a period for $f = 1.62$ Hz ($f_r = 1.1$).

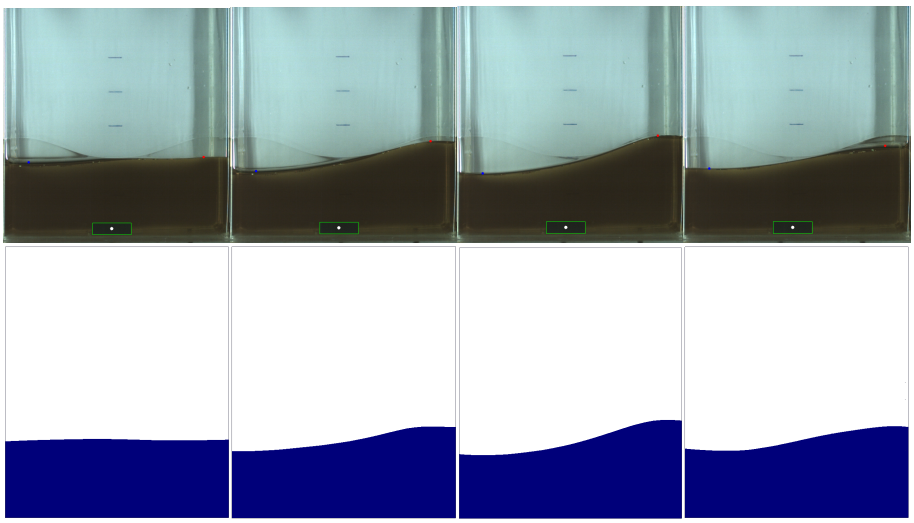

Figure 21: Free surface evolution in a period for $f = 1.69$ Hz ($f_r = 1.15$)

In all these analyses, the simulations satisfactorily match the experiments.

In Table 3, the total CPU time used to solve all cases for $f_r = 0.9$ are presented. All simulations were solved using four processors, and the simulation time was 40s. Note that for $M1$ and $dt = 0.005$s, the 8000 time steps only require 192s of total CPU time with an acceptable solution even for a case near the first mode.

Total CPU time	$dt = 0.005$s	$dt = 0.0025$s	$dt = 0.00125$s
$M1$	192s	387s	777s
$M2$	367s	705s	1400s
$M3$	390s	759s	1457s

Table 3: Total CPU time used in the case of $f = 1.32Hz$ ($f_r = 0.9$) to solve 40s of simulation.

6. Conclusions

An exhaustive experimental and numerical analysis of the sloshing of a squared tank partially filled with a domestic vegetable oil has been presented. Specifically, an oil sloshing of square tanks experiment is reported. With the aim to confirm the experimental data, free surface evolution has been measured using two techniques: ultrasonic sensors and image capturing. Material properties are also experimentally determined. From the numerical point of view, a variational multi-scale stabilized finite element method with a level set technique developed in an adaptive meshes using a Fixed-Mesh Arbitrary Eulerian Lagrangian method, has been presented.

The experimental trends confirm that maximum and minimum wave amplitudes:

- increase with the amplitude of the imposed motion for a given frequency of the imposed motion.
- increase with the filling depth for a given imposed motion, and they tends to reach similar values for the higher filling depth, i.e., the wave pattern started to be independent of the filling depth.
- nonlinearities, expressed by the ratio between maximum and minimum wave amplitudes, are strong at the studied low filling depth.

From the numerical analyses, the observed aspects can be summarized as:

- mesh and time step size refinement reveal practically independent numerical behaviour, but better results are computed with their small sizes near resonant conditions.
- the adaptivity procedure warrants good results also when relatively coarse meshes are used, on benefit of the computational time.
- the results obtained in the simulation satisfactory adjust the experimental data validating the proposed numerical model.

References

[1] S. Jiang, Z. Wang, G. Zhou, and W. Yang, "An implicit control-volume finite element method and its time step strategies for injection molding simulation," *Computers & Chemical Engineering*, vol. 31, no. 11, pp. 1407 – 1418, 2007.

[2] J.-D. Yu, S. Sakai, and J. Sethian, "Two-phase viscoelastic jetting," *Journal of Computational Physics*, vol. 220, no. 2, pp. 568 – 585, 2007.

[3] J. Favero, A. Secchi, N. Cardozo, and H. Jasak, "Viscoelastic fluid analysis in internal and in free surface flows using the software openfoam," *Computers & Chemical Engineering*, vol. 34, no. 12, pp. 1984 – 1993, 2010. 10th International Symposium on Process Systems Engineering, Salvador, Bahia, Brasil, 16-20 August 2009.

[4] M. Cruchaga, L. Battaglia, M. Storti, and J. D'Elía, "Numerical modeling and experimental validation of free surface flow problems," *Archives of Computational Methods in Engineering*, vol. 23, pp. 139–169, Mar 2016.

[5] J. Baiges, R. Codina, A. Pont, and E. Castillo, "An adaptive fixed-mesh ALE method for free surface flows," *Computer Methods in Applied Mechanics and Engineering*, vol. 313, pp. 159 – 188, 2017.

[6] E. Castillo, J. Baiges, and R. Codina, "Approximation of the two-fluid flow problem for viscoelastic fluids using the level set method and pressure enriched finite element shape functions," *Journal of Non-Newtonian Fluid Mechanics*, vol. 225, pp. 37–53, 2015.

[7] N. O. Moraga, E. F. Castillo, and C. P. Garrido, "Non Newtonian annular alloy solidification in mould," *Heat and Mass Transfer*, vol. 48, pp. 1415–1424, Aug 2012.

[8] A. Escobar, D. Celentano, M. Cruchaga, J. Lacaze, B. Schulz, P. Dardati, and A. Parada, "Experimental and numerical analysis of effect of cooling rate on thermal-microstructural response of spheroidal graphite cast iron solidification," *International Journal of Cast Metals Research*, vol. 27, no. 3, pp. 176–186, 2014.

[9] L. Benedetti, M. Cervera, and M. Chiumenti, "High-fidelity prediction of crack formation in 2D and 3D pullout tests," *Computers & Structures*, vol. 172, pp. 93 – 109, 2016.

[10] J. Baiges and R. Codina, "Variational multiscale error estimators for solid mechanics adaptive simulations: An orthogonal subgrid scale approach," *Computer Methods in Applied Mechanics and Engineering*, vol. 325, pp. 37 – 55, 2017.

[11] M. Moure, F. Otero, S. García-Castillo, S. Sánchez-Sáez, E. Barbero, and E. Barbero, "Damage evolution in open-hole laminated composite plates subjected to in-plane loads," *Composite Structures*, vol. 133, pp. 1048 – 1057, 2015.

[12] A. Huerta and W. K. Liu, "Viscous flow with large free surface motion," *Computer Methods in Applied Mechanics and Engineering*, vol. 69, no. 3, pp. 277 – 324, 1988.

[13] T. J. Hughes, W. K. Liu, and T. K. Zimmermann, "Lagrangian-Eulerian finite element formulation for incompressible viscous flows," *Computer Methods in Applied Mechanics and Engineering*, vol. 29, no. 3, pp. 329 – 349, 1981.

[14] P. Díez and A. Huerta, "A unified approach to remeshing strategies for finite element h-adaptivity," *Computer Methods in Applied Mechanics and Engineering*, vol. 176, no. 1, pp. 215 – 229, 1999.

[15] H. Askes and L. J. Sluys, "Remeshing strategies for adaptive ALE analysis of strain localisation," *European Journal of Mechanics - A/Solids*, vol. 19, no. 3, pp. 447 – 467, 2000.

[16] R. Codina, G. Houzeaux, H. Coppola-Owen, and J. Baiges, "The fixed-mesh ALE approach for the numerical approximation of flows in moving domains," *Journal of Computational Physics*, vol. 228, no. 5, pp. 1591 – 1611, 2009.

[17] H. Coppola-Owen and R. Codina, "A free surface finite element model for low Froude number mould filling problems on fixed meshes," *International Journal for Numerical Methods in Fluids*, vol. 66, no. 7, pp. 833–851, 2011.

[18] J. Baiges, R. Codina, and H. Coppola-Owen, "The Fixed-Mesh ALE approach for the numerical simulation of floating solids," *International Journal for Numerical Methods in Fluids*, vol. 67, no. 8, pp. 1004–1023, 2011.

[19] M. A. Cruchaga, R. S. Reinoso, M. A. Storti, D. J. Celentano, and T. E. Tezduyar, "Finite element computation and experimental validation of sloshing in rectangular tanks," *Computational Mechanics*, vol. 52, pp. 1301–1312, Dec 2013.

[20] L. Battaglia, M. Cruchaga, M. Storti, J. D'Elía, J. N. Aedo, and R. Reinoso, "Numerical modelling of 3d sloshing experiments in rectangular tanks," *Applied Mathematical Modelling*, vol. 59, pp. 357–378, 2018.

[21] C. Hirt, A. Amsden, and J. Cook, "An Arbitrary Lagrangian-Eulerian computing method for all flow speeds," *Journal of Computational Physics*, vol. 135, no. 2, pp. 203 – 216, 1997.

[22] T. J. Hughes, G. R. Feijóo, L. Mazzei, and J.-B. Quincy, "The variational multiscale method-a paradigm for computational mechanics," *Computer Methods in Applied Mechanics and Engineering*, vol. 166, no. 1-2, pp. 3–24, 1998.

[23] R. Codina, "A stabilized finite element method for generalized stationary incompressible flows," *Computer Methods in Applied Mechanics and Engineering*, vol. 190, no. 20-21, pp. 2681–2706, 2001.

[24] R. Codina, J. Principe, O. Guasch, and S. Badia, "Time dependent subscales in the stabilized finite element approximation of incompressible flow problems," *Computer Methods in Applied Mechanics and Engineering*, vol. 196, no. 21-24, pp. 2413–2430, 2007.

[25] R. Codina, "Analysis of a stabilized finite element approximation of the Oseen equations using orthogonal subscales," *Applied Numerical Mathematics*, vol. 58, no. 3, pp. 264–283, 2008.

[26] E. Burman and M. A. Fernández, "An unfitted Nitsche method for incompressible fluid-structure interaction using overlapping meshes," *Computer Methods in Applied Mechanics and Engineering*, vol. 279, pp. 497 – 514, 2014.

[27] Burman, Erik and Hansbo, Peter, "Fictitious domain methods using cut elements: Iii. a stabilized Nitsche method for stokes problem," *ESAIM: M2AN*, vol. 48, no. 3, pp. 859–874, 2014.

[28] E. Burman, "Ghost penalty," *Comptes Rendus Mathematique*, vol. 348, no. 21, pp. 1217 – 1220, 2010.

[29] A. N. Brooks and T. J. Hughes, "Streamline upwind/Petrov-Galerkin formulations for convection dominated flows with particular emphasis on the incompressible navier-stokes equations," *Computer Methods in Applied Mechanics and Engineering*, vol. 32, no. 1, pp. 199 – 259, 1982.

[30] J. Baiges and C. Bayona, "Refficientlib: An efficient load-rebalanced adaptive mesh refinement algorithm for high-performance computational physics meshes," *SIAM Journal on Scientific Computing*, vol. 39, no. 2, pp. C65–C95, 2017.

[31] Quanser, "STII Manual," *On line access:www.quanser.com*, 2017.

[32] B. Engineering, "U-GAGETM S18U Series Sensors with Analog Output," *On line access:www.bannerengineering.com*, 2017.

[33] A. Technologies, "Q-PRI High Speed Camera," *On line access:www.aostechnologies.com*, 2017.

[34] OpenCV, "The OpenCV Reference manual," *On line access:opencv.org*, 2017.

[35] O. Faltinsen, O. Rognebakke, I. Lukovsky, and A. Timokha, "Multidimensional modal analysis of nonlinear sloshing in a rectangular tank with finite water depth," *Journal of Fluid Mechanics*, vol. 407, pp. 201–234, 2000.

[36] B. Esteban, J.-R. Riba, G. Baquero, A. Rius, and R. Puig, "Temperature dependence of density and viscosity of vegetable oils," *Biomass and bioenergy*, vol. 42, pp. 164–171, 2012.